Surface Air Temperature in Complex Terrain: Daily Predictions of Fine-Scale (30 m) Temperature in the Snake Range, Nevada, USA

Andrew P. Vitale* , Thomas P. Albright, and Stephanie A. McAfee

Department of Geography, University of Nevada, Reno, Reno, Nevada, United States of America

Peter J. Weisberg

Department of Natural Resources and Environmental Science, University of Nevada, Reno, Reno, Nevada, United States of America

**Corresponding author address:* Andrew P. Vitale, Department of Geography, University of Nevada, Reno, 1664 N. Virginia St., Reno, NV 89557.

E-mail: andrew.vitale@nevada.unr.edu

ABSTRACT

Air temperature is arguably the most important component of the mountain climate, and authors have been studying it for centuries. Recently, researchers have used arrays of inexpensive temperature sensors to observe and model temperature across the landscape, largely focusing on landscape features as drivers of temperature. This paper shows that near-surface minimum and maximum temperature vary greatly across the landscape in the Snake Range, and that the effect of landscape features on temperature distribution changes with weather conditions and season. To this end, we conducted an Empirical Orthogonal Function analysis of gridded Sea Level Pressure (SLP) from 1951-2014, which identified a mode of variability that well describes synoptic weather in our study area. Synoptic weather and NCEP Reanalysis 1 derived regional air temperature were linked with a network of 40 temperature sensors spanning June 2013-2014 and GIS derived landscape variables to create hierarchical-mixed effects models of daily minimum and maximum temperature in the Snake Range. Minimum temperatures were mostly linked to elevation and the shape of the landscape, as cold air drainage is a major climatic component in the Snake Range. Maximum temperature is largely related to solar irradiance and elevation, with a large seasonal component. We used these models to create 373 maps of daily minimum and maximum temperature in the Snake Range at the spatial scale of 30 m. The map predictions were validated using 4 independent weather stations, and overall bias for minimum and maximum temperature were 0.69 and -1.92 °C, respectively.

1. Introduction

Air temperature is an essential component of climate in mountainous areas (Lookingbill and Urban 2003; Barry 2008). It effects many processes such as the timing of snow melt, evapotranspiration, photosynthesis, drought tolerance, carbon fixation, and the distribution of plants and animals (Cabrera et al. 1998; Barry 2008; Adams et al. 2009; Geiger et al. 2009; Crimmins et al. 2011). Surface air temperature is frequently a focal point of climate change impact studies and resource management alike (Diaz et al. 2003; Millar et al. 2007), highlighting the importance of understanding and accurately representing this dynamic environmental parameter across the landscape.

Near-surface air temperature gradients tend to vary over short distances and with the seasons in mountain settings, making for a complex spatio-temporal pattern. Patterns of near-surface air temperature are driven by both regional and landscape-scale characteristics (Steinhauser 1967; Dobrowski et al. 2009). In the context of this work, regional-scale characteristics refers to synoptic-scale weather patterns and larger-scale geographic features such as the orientation of mountain ranges, latitude, and distance to significant water bodies. Landscape-scale characteristics refers to site specific conditions at the scale of the watershed (Dobrowski et al. 2009). While elevation is often reasonably predictive of surface air temperature (temperature decreases with increasing elevation), this relationship alone does not account for the variation of temperature in mountain environments, as fine-scale variations in solar heat transfer occur due to varying landscape-scale characteristics such as the terrain slope and orientation, shading from local vegetation, and variation in evapotranspiration across the landscape, which can have profound effects on surface air temperature [THIS NEEDS A CITATION OR 8]. The influence of these landscape-scale characteristics are dynamic through time, changing with the seasons and synoptic weather conditions.

While the need to understand near-surface air temperature in mountain environments is clear, it has proven very difficult to accurately estimate temperature patterns in complex terrain. A common method of estimation has been the use of an adiabatic lapse rate of -6.5 °C km^{-1} (henceforth standard lapse rate) (e.g. Martinec and Rango 1986). This method describes an average that fails to account for spatial differences in temperature driven by topography, vegetation, substrate, and many other factors (Barry 2008; Geiger et al. 2009), most of which vary greatly at different locations. Moreover, the use of a standard lapse rate fails to account for temporal variation in the relationship between elevation and near-surface air temperature, which is known to vary greatly on both diurnal and seasonal time scales. Lapse rates tend to exhibit a greater increase in temperature with elevation during the day than at night and they also tend to exhibit seasonal variations, with steeper lapse rates (greater decrease in temperature with elevation) during the warmer months than the cold months (Barry 2008; Rolland 2003; Pepin et al. 1999).

Synoptic weather also plays a large role in the variation of near-surface air temperature in mountain environments, which can be inferred from studies focusing on variation in lapse rates with synoptic weather conditions. Blandford et al. (2008) found that lapse rates for daily maximum temperature (T_{max}) and minimum temperatures (T_{min}) varied with synoptic conditions in the mountains of south-central Idaho, though they found the relationship with T_{max} lapse rates and synoptic conditions was more tenuous than that of T_{min} lapse rates. Their study showed that lapse rates were generally steeper while warmer air masses were present, while more shallow lapse rates were observed during the presence of dry air masses. They found that the largest diurnal fluctuations in lapse rates occurred during dry tropical air masses, largely due to the clear skies associated with these synoptic conditions. When examining the differences in synoptic conditions' effects on lapse rates during different seasons, they found that the effects of synoptic conditions were generally consistent. Another study conducted by Pepin et al. (1999) found that synoptic conditions also have a large effect on lapse rates in northern England, with anticyclones leading to larger differences between T_{max} and T_{min} lapse rates. Anticyclones are generally associated with calm weather and clear sky conditions. Calm conditions and clear skies typically lead to cold air drainage due to the escape of long wave radiation since there is no cloud cover to trap the radiation, leading to lower temperatures at the valley floor than at higher terrain. Furthermore, T_{max} rates tend to increase under these conditions, as more short wave radiation reaches the ground surface under clear skies.

Methods other than standard lapse rates have been developed to estimate surface air temperature, particularly in the form of gridded datasets based on station observations (e.g. PRISM, DAYMET, WorldClim) (Daly et al. 2008; Thornton et al. 1997; Hijmans et al. 2005). Some gridded datasets account for topographically mediated temperature patterns and consider the effects of regional-scale physiographic features (e.g. mountain ranges, temperature inversions, and distance to coast) in their temperature interpolation algorithms.

While the available gridded products are useful for many applications, their use in mountainous, landscape-scale study areas is limited by their weather station inputs. Weather stations are sparse in mountain environments, thus most weather station observations come from valley locations in the United States of America (USA) (Hijmans et al. 2005; Myrick and Horel 2008; Horel and Dong 2010). The limited sampling in mountain ranges fails to quantifiably observe topographically driven temperature regimes at the landscape-scale, which are known to be influential in temperature patterns that are relevant to landscape-scale biophysical processes (Lundquist and Cayan 2007; Barry 2008; Geiger et al. 2009; Crimmins et al. 2011; Ashcroft et al. 2012).

There have been numerous efforts to characterize temperature at scales that more completely account for landscape-scale drivers of near-surface air temperature (Lundquist and Cayan 2007; Holden et al. 2011; Lookingbill and Urban 2003; Ashcroft and Gollan 2011; Fridley 2009). These studies have employed vastly different methods to analyze networks of inexpensive temperature sensors in mountainous environments, and they share both similarities and differences in their findings. Lundquist and Cayan (2007) and Holden et al. (2011) found that synoptic conditions were important drivers of near-surface air temperature in the Sierra Nevada of California and two mountain ranges in northern Idaho, respectively. Lookingbill and Urban (2003) and Fridley (2009) found significant effects of distance to streams on near-surface air temperatures, while Holden et al. (2011), Ashcroft and Gollan (2011), and Lundquist and Cayan (2007) did not report effects of this variable. In general, researchers have had success in characterizing and mapping near-surface air temperatures at their respective study locations, highlighting similarities and differences in the drivers of near-surface air temperature at different locations across the globe when considering the landcape-scale. One difficulty in comparing existing landscape-scale near-surface air temperature studies is the difference in both study design (e.g. sensor height above ground, sampling locations, etc.) and statistical methods used. Thus, further study in new locations is still warranted and should ideally be described in context of the existing literature.

The goals of this study are to: (1) observe and describe how near-surface air temperature (2 m above the ground surface) varies both spatially and temporally in a topographically complex landscape characteristic of Great Basin mountain ranges; (2) quantify the effects of synoptic weather conditions on spatial variation in near-surface air temperature; (3) demonstrate the ability to construct inferential and predictive statistical models of site-specific near-surface T_{max} and T_{min} in a remote, highly instrumented watershed. To achieve these goals, we have deployed the Snake Range Sensor Network (SRSN), a network of 40 temperature sensors, (Fig. 1) in and around Great Basin National Park, and have obtained daily T_{max} and T_{min} from the sensors for the period June 17, 2013 to June 24, 2014. We have used methods similar to Fridley (2009) by creating multilevel, mixed-effect linear models based on maximum likelihood, as these models provide the flexibility of describing hierarchically structured landscape processes while accounting for spatio-temporal autocorrelation. The model coefficients are interpreted to obtain a better understanding of how near-surface air temperature varies in the study site. We validate the hierarchical mixed effects models using the independent Nevada Climate-echohydrological Assessment Network (NevCAN) stations in the study site, and finally, produce fine scale maps of daily T_{max} and T_{min} for the study period using a GIS framework.

2. Methods

a. Study Site

Our study site (Fig. 1) is located near and within Great Basin National Park (GBNP), Nevada, USA on the west slope of the Snake Range of eastern Nevada. Typical of the Great Basin, our study site consists of a long, broad, north-south oriented valley with steep mountains to both the east and west. The average elevation of the valley is approximately 1500 m above mean sea level (AMSL), while the highest point in our study site, Mount Washington, is about 3550 m AMSL. Our study site surrounds four weather stations (Sage, PJ, Montane, Subalpine) (Fig. 1), which are apart of the Nevada Climate-Ecohydrological Assessment Network (NevCAN) (http://sensor.nevada.edu). These stations are all sited within different dominant vegetation types. From west to east, the Snake Range study site includes the sagebrush zone (dominant species: *Artemesia tridentata*), the Pinyon-Juniper zone (dominant species: *Pinus monophylla*, *Juniperus osteosperma*), the montane zone (dominant species: *Abies concolor*, *Pinus flexilis*), and the subalpine zone (dominant species: *Pinus longaeva*, *Pinus flexilis*). A significant portion of the study site near the subalpine zone burned within the past 15 years (10%). Precipitation in the area is mostly dominated by Pacific frontal storm systems in the winter, but isolated to scattered thunderstorms are also common in the summer. The annual atmospheric lapse rate for the area was calculated as -5.9 °C km^{-1} +/- 0.5 °C for the 2012 water year (2011 Oct 1 to 2012 Sep 30) (Mensing et al. 2013).

b. Snake Range Sensor Network

We installed the Snake Range Sensor Network (SRSN) a network of 40 LogTag Trix 16 temperature sensors along an elevational gradient in the west slope of the Snake Range. The sensors are housed in inexpensive radiation shields constructed of easily sourced materials, as outlined by Holden et al. (2013). The sensors were placed 2 m above the ground surface, affixed to trees when available and attached to PVC poles that are strapped to shrubs when no trees were nearby

Sampling locations were determined by a GIS analysis, the aim of which was to ensure sampling a range of topographic and topoclimatic conditions. The analysis consisted of splitting the mountain into four elevation zones (1500-2000 m; 2000-2500 m; 2500-2000 m; 3000-3500 m). For each elevation zone, we used the ESRI ArcGIS 10.0 Isocluster tool to generate 10 unique combinations of variables thought to influence topoclimate including slope, slope position, heat load index (McCune and Keon 2002), and the National Land Cover Dataset (NLCD) 2006 canopy cover dataset [CITE NLCD], which left us with a total of 40 unique clusters (10 clusters in each of the 4 zones), with each cluster occurring numerous times within the spatial extent of the analysis as polygons. The Isocluster tool works by use of the migrating means technique, which separates the values of all cells into unimodal groups that are distinct from one another. Minimum euclidean distance to arbitrarily defined means is calculated for each cluster, and the cells are assigned to the clusters accordingly. New means are calculated for each cluster, and the process is repeated until the user defined number of iterations is reached (ESRI 2014). To determine the final sensor location, we generated spatially random points within the 40 polygons that encompassed the largest surface area of the 40 clusters, as the largest surface area polygon is most likely to represent the combination of the input data that the Isocluster algorithm identified. The resulting spatial distribution of the SRSN sensors is shown in Figure 1.

c. Predictor Variables: Synoptic Weather

1) Free Air Temperature

As one of the underlying interests of this study is characterizing terrain's ability to create local deviations in temperature from the free-air, we need an effective means of representing free-air temperature for our study site. Our study site lies within a single grid cell of the NCEP/NCAR Reanalysis 1 (Kalnay et al. 1996). The Reanalysis 1 project assimilates data from a number of sources, including land, ship, satellite, radiosondes, and others. Assimilations are produced 4-times daily, as are daily and monthly means. We use daily mean air temperature at the 750 hPa level to indicated free-air temperature at our study site. This pressure level is generally associated with an elevation of approximately 3000 m AMSL, thus it should have minimal effects from the mountains in the area. The exact height AMSL of this variable varies on a daily basis.

2) Sea Level Pressure: Empirical Orthogonal Functions

It is known that synoptic weather patterns have a great influence on near-surface air temperature in areas of complex terrain. In our western Nevada study site, for example, both T_{max} and T_{min} can become cooler along the lower elevation valley floor than the summit of Mount Washington. These temperature inversions, which add a large amount of complexity to understanding and predicting near-surface air temperature, occur more commonly in the Snake Range during anticyclonic patterns, which are typically associated with high pressure systems. Inversions tend to form due to radiative cooling of the ground surface, which in turn cools the air. The more dense, cooler air then sinks to lower elevation, concave terrain features, like the long, broad valleys of the Great

Basin. Conversely, cyclonic conditions lead to a greater mixing of the boundary layer with the free atmosphere, thus a linear decrease of temperature with increasing elevation is typically observed under cyclonic conditions. It is thought that T_{min} has a greater response to local scale topography, while T_{max} is more influenced by synoptic scale atmospheric conditions (Lundquist et al. 2008; Lundquist and Cayan 2007; Pepin et al. 2011).

There is a long history of using empirical orthogonal functions (EOFs), also commonly referred to as principle components analysis (PCA), to better understand two dimensional fields of meteorological data (Hannachi et al. 2007). EOFs work to decompose a dataset, a space by time matrix in the case of meteorological fields, into new variables. The new variables are orthogonal to one another, thus uncorrelated, account for much of the variance in the original data, and will be linear combinations of the original data (Hannachi et al. 2007).

Based on the variation in lapse rates and near-surface air temperature that have been related to synoptic weather conditions in our study site and locations with similarly complex terrain (Lundquist et al. 2008; Lundquist and Cayan 2007; Pepin et al. 2011; Blandford et al. 2008), we suspected synoptic conditions would have a strong effect on both T_{max} and T_{min} in the area of the SRSN. To obtain a better understanding of synoptic weather in our study site, we retrieved daily average sea level pressure (SLP) grids (2.5° resolution) from the NCEP/NCAR Reanalysis 1 (Kalnay et al. 1996) for the period of January 1, 1958 to September 24, 2014 in the spatial domain of approximately 176°W to 98°W and 16°N to 68°N. Using the raster package in R (Hijmans 2014), we first reprojected the data from a geographic coordinate system (longitude/latitude) to a planer equidistant projection using a bilinear interpolation, as this helps to account for decreasing surface area of longitude/latitude grid cells as you travel away from the equator. We then calculated SLP anomalies on the re-gridded dataset by subtracting the mean for the entire period from each day's assimilation. EOFs and their associated temporal variation (principle components or

PCs) were calculated for the entire period using the spacetime package (Pebesma 2012; Bivand et al. 2013) in R (Figure 2 and Figure 3 respectively).

The most difficult portion of an EOF analysis is surely the interpretation. With careful consideration of both the EOFs (Figure 2) and their associated PC time series (Figure 3), we were able to identify interpretable modes of variability within SLP fields over the Eastern Pacific Ocean and the Western United States. In Figure 2, panel (a) represents the familiar pattern of SLP often referred to as the Aleutian Low. This EOF accounts for 36% of the variance in SLP anomalies (Table 1), and displays a highly seasonal trend with positive PC values in the winter, and negative PC values in the summer (Figure 3 (a)).

The second EOF (Figure 2 (b)) represents anomalously high SLP over the Pacific and anomalously low SLP over the northeastern portion of the analysis domain. This mode of SLP variability is associated with the formation and movement of large frontal storms from the Pacific over the northern portion of the domain, while the inverse of this pattern is associated with the formation of a high pressure ridge off the coast of Western North America. Again, this EOF displays more variation during the winter season (Figure 3 (b)) and a largely seasonal pattern. EOF2 accounts for 22% of the variation observed in SLP anomalies during our study domain (Table 1).

The third EOF (Figure 2 (c)) accounts for less of the variation in SLP anomalies at 10% (Table 1). The pattern identified here reflects anomalously low SLP off the coast of the Western United States, and when in the negative phase, an anomalously high SLP occurs off the coast of the Western United States. While there is a fair amount of intra-annual variability of this pattern (Figure 3 (c)), it appears to evolve on a timescale measure in weeks rather than days.

Finally, the fourth EOF presented here (Figure 2 (d)) accounts for 8% (Table 1) of the total variance in SLP anomalies in the study domain. This pattern displays a strong correlation with the formation and passage of low pressure systems over the western portion of the United

States. Moreover, the formation of Colorado Clipper systems (low pressure systems that form in southeastern Colorado and track to the northeast across the U.S. over the course of several days (http://w1.weather.gov/glossary/index.php?word=Colorado+low [BEEF UP THIS CITATION]) is predominately associated with positive values of PC4. PC4 shows predominately daily variation in its magnitude and sign (Figure 3 (d)), indicating this mode of SLP identified by the EOF analysis is indicative of changes in synoptic weather patterns on a time scale that is directly comparable to variations in daily near-surface air temperature. As a first-order test of this assertion, we calculated daily lapse rates for T_{min} and T_{max} from the SRSN data. The lapse rates were then compared with variations in PC4 for the same period using Pearson's Correlation Coefficient, and we found that PC4 is inversely proportional to T_{min} and T_{max} lapse rates (r = -0.41 and r = -0.40, respectively). Thus, we decided to consider PC4 as a predictor variable in our hierarchical mixed-effects models for near-surface air temperature at the study site in an attempt to quantify the effects of synoptic scale circulations on temperature patterns in the region.

d. Predictor Variables: Topography

There have been a number of studies conducted which have successfully associated processes that drive landscape- scale near-surface air temperature with easily measured features of the landscape (e.g. elevation, slope, topographic position indices) (Fridley 2009; Dobrowski et al. 2009; Ashcroft and Gollan 2011). Rather than focusing on a review of all landscape-scale processes that are relevant to near-surface air temperature, we present a brief description of the main landscape feature we expect to contribute to T_{min} and T_{max} at our study site.

Maximum temperatures tend to vary based on the amount of direct beam solar radiation that is received at the location (Geiger et al. 2009). This is mostly controlled by the slope and aspect of the surface in complex terrain, with additional influences due to shading caused by adjacent topographic features. The radiation warms up the land surface, which in turn acts to warm the near- surface air (Geiger et al. 2009).

Minimum temperatures are indirectly related to daily solar energy balances, but are influenced more directly by the movement of cold air over the landscape (i.e. katbatic winds and cold air drainage). The loss of longwave radiation from the ground surface is an important process in terms of T_{min}, and is largely determined by slope angle and vegetation cover (Fridley 2009; Geiger et al. 2009).

For our study site, we suspect that the principle landscape-scale drivers of near-surface air temperature are incoming solar radiation, cold air drainage (more commonly in T_{min} than T_{max}), and evapotranspiration. GRASS GIS 6.4 [ADD BIBTEX ENTRY] has implemented the r.sun algorithm, which calculates direct beam, diffuse, and reflected radiation for a given raster cell on a given day from an input digital elevation model (DEM). The model allows for consideration of latitude, shading from nearby terrain features, day of year, slope orientation, and slope angle in its estimate of solar irradiance (Wm^2). A preliminary analysis was conducted using a similar metric, the heat load index (McCune and Keon 2002), but early indications pointed towards the GRASS r.sun algorithm as a superior method for estimating clear-sky solar irradiance, hence its inclusion in our T_{max} and T_{min} models.

Cold air drainage has been represented by the terrain convergence index (TCI), which can also be easily calculated in GRASS GIS (r.terraflow algorithm). This algorithm calculates the flow of a fluid over terrain, requiring only a DEM as input. The most intuitive application of this tool is in understanding the flow patterns of water over terrain. TCI at our study site ranged in values from 2.1-17.1, where higher values are associated with concave terrain features. As cold, dense air tends to respond similarly to water, we anticipate areas of high TCI values are more likely to encounter cold air drainage. Dobrowski et al. (2009) successfully used TCI as a proxy to cold air drainage.

e. Model Construction

Similar to Fridley (2009), we have opted to use a mixed-effects hierarchical linear model structure to predict T_{min} and T_{max} from synoptic weather conditions (we use NCEP/NCAR Reanalysis 1 rather than local weather stations) and GIS derived predictor variables. These models are effective at representing nested data, as they incorporate both fixed effects and random effects. Fixed effects are measurable environmental variables, while random effects are unmeasured noise associated with individual samples or groups of samples [CITE PINHERO BATES HERE]. Given the correlation of temperature within our study site through both space and time, mixed effect models are further justified, as they provide the benefit of describing nested covariance structures. In the case of our study, temporal variation is nested within each spatial location (i.e. each sensor location as seen in Figure 1). The sampling design of this study results in a model of two nested levels. The first level is the daily variation of temperature at each site. We have observed T_{max} and T_{min} over the course of 373 days (17 June 2013 to 24 June 2014). The second level of the model describes variation across space (i.e. the mean temperature over the 373 days of observations varies as a function of spatial location on the landscape). The mixed-effects hierarchical linear model structure allows for random effects to be associated with each sample unit (here days within location and each individual location). The random effects have the property of describing variance in the response that can not be attributed to the environmental variables included within the model (i.e. the fixed effects), thus can remove noise that would effect model extrapolation to the landscape. That is to say, the random effects can help to remove unwanted noise from the global coefficient estimates, as only these estimates can be used in extrapolation of the model to the landscape.

A more detailed description of the model fitting procedure and the final fitted models is described in Supplement A. We fit the models with R version 3.1.2 (R Core Team 2014). Both the ”nlme” (Pinheiro et al. 2014) package and the ”lme4” (Bates, D and Maechler, M and Bolker, B and Walker, S 2014) package were used to fit the hierarchical models, and an R script that goes through the model fitting procedures is included as Supplement B. Model coefficients were fit with maximum likelihood, and models were compared using Aikake's information criterion (AIC) from log-likelihood tests. As further outlined in Supplement A, much of the spatial autocorrelation is addressed by inclusion of random effects in the final models. Temporal autocorrelation is also addressed by random effects. Models were also fit with an exponentially decaying temporal covariance structure, but the added complexity did not appear to be required as indicated by log liklihood tests and AIC.

f. Model Validation and Mapping

To validate our models of T_{max} and T_{min} for the entirety of the mapped region, we downloaded daily maximum and minimum temperature at 2 m above the ground surface from the NevCAN stations in the region (Sagebrush, PJ, Montane, Subalpine; Figure 1). The models were used to predict T_{max} and T_{min} for these locations, and we calculated model bias (difference between predicted and observed temperature), accuracy (mean absolute error [MAE], calculated as the difference between the predicted and observed temperature after all values have been made positive), and root mean squared error ([RMSE], calculated as the square root of the mean bias squared).

The fixed-effect coefficients of the models were then used to predict temperature for a grid with square cells of approximately 30 m for the entire study area during the entire period of observation (17 June 2013 to 24 June 2014). Maps were generated within R, using the ”raster” (Hijmans

2014) package to handle the spatial data and apply the fixed effects to the GIS predictor variables. Predicted T_{max} and T_{min} are available as GeoTIFF files in supplement C.

3. Results

a. Synoptic Patterns in the Snake Range

Large variations in average daily temperature of the free air mass (i.e. NCEP Reanalysis 1 daily average temperature at 700 hPa) were observed in the snake range between 17 June 2013 and 24 June 2014. The regional temperature value of 19.3 °C occurred on 1 July 2013, while the minimum value of -20.6 °C occurred on 5 December 2013. As seen in Figure 4, this minimum value is substantially lower than the majority of winter days in the region. It occurred during what can be thought of as an extreme cold event (a ”cold snap”) that spanned approximately 4 December 2013 to 9 December 2013. Average temperature in the region dropped from -4.9 °C to -17.3 °C in the span of 24 hours. Between 9 December 2013 and 10 December 2013 temperatures warmed in a similarly sudden manner, with average daily temperature jumping from -17.7 °C to -8.4 °C in a 24 hour span. As seen in Figure 3, PC4 (an indicator of low pressure system passage, with positive values representing low pressure and negative values representing high pressure) shows the greatest variation in the winter months, which is consistent with the climatology of the region. Throughout our record, the cold events are typically preceeded by high values of PC4. For example, the maximum value of PC4 during the period of the SRSN occurred on 28 February 2014 with a value of 3.0. As seen in Figure 4, this date precedes the onset of a ”cold snap” in the Snake Range area, with temperatures dipping for a period of a few days. We interpret this pattern as a cold front moving through the area. The low pressure is indicated by PC4. Once the front clears, high pressure builds with a cold air mass in place, thus persistent low temperatures occur. A local maximum of PC4 also occurs prior to the 5 December 2013 ”cold snap”, as seen in Figures 3 and 4 and using the NCEP daily weather map tool (advance map by clicking ”NEXT DAY”; `http://www.hpc.ncep.noaa.gov/dailywxmap/index_20131203.html`).

b. Temperature Variation across the SRSN

1) Minimum Temperature

As seen in both Figures 4 and 5, there is a large amount of variation in minimum temperature across the SRSN. Typical of mountain environments, elevation is largely predictive of temperature. However, this relationship often breaks down, and other terrain factors have a large influence over the temperature experienced at a particular location. AIC tests were conducted using residuals from a linear mixed-effects model of T_{min}, allowing the intercept to randomly vary by month, using average monthly temperature for each site. Terrain slope better explained the residuals when compared to TCI and NLCD canopy cover. The relationship between residual minimum temperature and slope is fairly constant throughout the course of the year, displaying larger variance at lower slope angles and a fairly consistent relationship across months with a slightly steeper relationship in the winter months(results not shown).

Conversely, the relationship between TCI and residual minimum temperature shows large variability across months (Figure 5). The winter months show a strong negative relationship between residual minimum temperature and TCI, with higher values of TCI generally associated with negative T_{min} residuals. This indicates that areas with high TCI values (valley floors) are experiencing colder than expected T_{min} values when only elevation is considered. While this relationship holds true for the winter months, there does not appear to be a significant relationship in the spring, summer, or fall.

2) Maximum Temperature

Figures 4 and 6 both show the variation that is present in daily maximum temperature across the SRSN. Elevation is an even stronger predictor of maximum temperature in the Snake Range than it is for minimum temperature. AIC tests were conducted on the residuals of a linear mixed-effects model of T_{max}, allowing the intercept to randomly vary by month, using average monthly temperature for each site. Again, similar to minimum temperature, terrain slope best explained the residuals of the maximum temperature model. The strength of this relationship varies by month, with the strongest positive linear relationship occurring in the winter months, when inversions are most likely to form. As seen in Figure 6, the residuals of maximum temperature predicted by elevation are most variable in winter, and closest to 0 in the summer months.

c. Model Performance and Validation

The model bias, mean absolute error (MAE), and root mean square error (RMSE) for the maximum and minimum daily temperature hierarchical mixed-effects models are shown in Table 5, Table 6, and Table 7, respectively. These tables show the performance of the T_{min} and T_{max} models for each month of the record as well as at 4 separate NevCAN sites, which are associated with different vegetation types and distinct elevations (Figure 1). The bias for the T_{min} model is visualized in Figure 7 and the T_{max} model bias is visualized in Figure 8.

The T_{min} model displayed a relatively small bias when averaged over sites and months of 0.69 °C (Table 5). Bias was relatively low for the Sage (0.85 °C), Montane (-0.05 °C), and Subalpine sites (-0.40 °C), while the Pinyon-Juniper (PJ) site had the highest overall bias (2.43 °C). In general, biases in the T_{min} model were highest in the winter months, when temperature inversions are most likely to occur. The lower elevation minimum temperature predictions show greater variation over time. The higher elevation Montane and Subalpine sites show relatively stable biases throughout the months.

The T_{max} model does not perform as well for the study site as does the T_{min} model (Table 5), with an overall bias across sites and times of -1.92 °C. The T_{max} model performs best at the Sage site over the course of the year, with an overall bias of only 0.05 °C. The PJ and Montane sites are both consistently large, negative biases, indicating that the model is under predicting temperature at those sites. The Subalpine site shows the greatest seasonal variation in bias for T_{max} predictions, with more negative biases in the summer months, and biases close to zero in the winter. Overall, the smallest bias for T_{max} are observed at the Sage and Subalpine sites (0.05 and -1.12 °C respectively), while the PJ and Montane sites display higher biases (-3.36 and -3.22 °C respectively).

Mean Absolute Error (MAE) of the T_{min} model was relatively low (1.92 °C, Table 6). The site displaying the highest MAE was the sage site (3.16 ° C), while the lowest MAE was observed at the Montane site (1.27 °C). The highest MAE by month at the Sage site is observed during the month of December (6.15 °C), while the lowest MAE is observed at the high elevation Subalpine site in August (0.80 °C). When comparing between sites, the PJ, Montane, and Subalpine sites show relatively stable MAEs throughout time, while the Sage site shows large variations over the course of the year.

MAE of the T_{max} model was higher than the T_{min} model (2.78 °C, Table 6), with consistently high MAE values across sites. The site with the lowest T_{max} MAE was the Sage site (2.27 °C). The Spring, and Summer MAE values for the Sage site were relatively consistent across time, while the Fall and Winter MAE values were higher and varied more significantly. The Sage site MAE in the month of December was particularly high (4.68 °C), while the MAE for the Sage site in

August was much lower (1.33 °C). The month with the highest MAE across sites (Overall in Table 6) was December (3.26 °C).

The root mean squared error (RMSE) of the T_{min} model was 2.70 °C (Table 7). The site with the highest RMSE was the Sage site (4.18 °C), which was a full 1.9 °C higher than the second highest RMSE at the PJ site (2.28 °C). December at the Sage site stands out with the highest RMSE (8.00 °C), and the sage site again shows lots of variation by month. The PJ, Montane, and Subalpine sites all show relatively stable RMSE values across months compared to the Sage site.

RMSE of the T_{max} model across time and space was slightly higher than the T_{min} model (3.35 °C, Table 7). RMSE values are more consistent for the T_{max} model than those of the T_{min} model, with the difference between the highest and lowest RMSE by site equaling 1.09 °C. The Sage site displays higher RMSE values during the winter, and the Montane site displays higher RMSE values in the Spring and Summer. The PJ site is relatively stable across months.

d. Temperature Distribution in the SRSN

We have created daily maps of minimum and maximum temperature for the entirety of the SRSN study site, with a total of 373 days of maps for each variable. Figure 9 (a) shows average minimum temperature for the month of December 2013 at the site, which was calculated by taking a simple mean of the daily minimum temperature predictions for that month. Figure 9 (b) shows average maximum temperature for the month of July 2013, which was calculated by taking a simple mean of maximum daily temperature predictions for that month. As seen in Figure 9, the pattern of minimum temperature, particularly in the winter months, is highly variable across the landscape. The correlation of the average temperature of each SRSN throughout the time period with elevation is low for T_{min} ($r = -0.65$), as valley locations are often as cold or colder than the summit of Mount Washington. Maximum temperature averaged across the time series at each site is more strongly correlated with elevation (r = -0.89). This is also apparent in Figure 9 (b), where it is clear that temperature increases linearly with elevation across the site.

4. Discussion

a. Variation of temperature in complex topography

The work presented here reiterates a theme that has become more common in the climate literature. near-surface air temperature in complex topography (like that found in the Snake Range) varies greatly over short distances. T_{min} tends to show substantial variation in values over very short distances (e.g. Figure 9a) and within short periods of time (e.g. Figure 1). The mosaic of minimum temperatures is very complicated at the landscape scale, and does not seem to follow a standard atmospheric lapse rate in our study area. The valley floors are often nearly as cold as the mountain summits, which can have profound implications for many applications that require information about minimum temperatures. Higher values of percent canopy cover tend to be associated with higher minimum temperatures, indicating that forested areas tend to buffer the region from extreme cold. While this phenomenon has been pointed out repeatedly throughout the literature [CITE - check out Fridley's references], it is often not accounted for in applied research.

T_{max} in our study site seems to more frequently display something approximating the standard atmospheric lapse rate. There is generally a consistent increase in maximum temperature with a decrease in elevation, and the regional air mass largely dictates where that temperature range is focused. While this is true throughout most of the year, there are still times (particularly in the winter) when T_{max} exhibits inversion conditions. Even at the hottest point of the day, the valley floor is cooler than higher elevations. Canopy cover also has a buffering effect on maximum temperatures, in that it can often produce cooler temperatures at elevations that would indicate otherwise. The complex spatio-temporal mosaic of both minimum and maximum temperature is quite difficult to quantify, thus the reliance in the past on simplified methods.

b. Effects of synoptic weather and seasonality on near-surface temperature

1) Minimum temperature

As expected, regional air temperature is the most predictive variable for the daily T_{min} maps in the study area. If the air mass is warm, all sites at the SRSN were slightly elevated. The inverse is also true, where cool regional air masses lead to cooler temperatures across all sites (Figure 4). While there may be better methods of indicating the regional air mass for some study locations, the remote nature of the Snake Range makes the NCEP Reanalysis 1 product well suited. The assimilation is consistent across the country, and the product is informed by satellite observations. If a radiosonde dataset is available in the area, it would be worth considering these data as an alternative to the Reanalysis. However, the closest radiosonde flights are in Reno, Nevada and Elko, Nevada, both of which are a sizable distance from the Snake Range.

T_{min} exhibited what can best be described as persistent temperature inversions throughout the study period. Cold air drainage is a major feature of the minimum temperature climate, as can be seen in Table 3. Not only is there a strong effect of elevation in predicting minimum temperature, but there is also quite a large effect of the quadratic of elevation. The quadratic term helps to account for the persistent cold air drainage observed at the study site. As seen in the left panel of Figure 10, minimum temperature tends to display no change in temperature with elevation until a certain elevation, where the decrease in temperature with elevation becomes linear. TCI and slope also help to account for the persistence of cold air drainage at the study site as indicated by their relatively high t values (Table 3). These two variables help to identify landscape features that are likely to allow dense, cold air to pool in convex or low slope features (i.e. areas with a high TCI value and/or low slope).

Another interesting feature that is shown here is the mobility of the elevation where the effect of cold air drainage is observed. The steady minimum temperature with increasing elevation seems to bounce around the 2,000-2,500 m mark (not shown). The variability of this elevation is inconsistent throughout the year, and we failed to model its mobility. The PJ NevCAN station is at an elevation of 2,200 m. In Figure 7, it is clear that T_{min} model predictions for the PJ station were very inconsistent throughout the year. Part of the high bias of the T_{min} model for this particular site is likely due to the fact that we are unable to estimate how thick the cold air drainage layer is on any given night with the predictor variables presented here. The depth and persistence of these layers at this site calls for more study.

Atmospheric mixing is another important component of the Snake Range climate, particularly in the winter months. Atmospheric mixing refers to the mixing of the near-surface air mass with the greater regional air mass. In the summer months, this can be achieved by convection where the air near the ground surface is warmed and rises. However, this process is limited in the summer due to lower sun angles and the complexity of the terrain. More of the landscape begins to experience ”deep shade”, that is to say that these areas receive no direct solar radiation throughout the course of the day. Thus, in the winter, atmospheric mixing is often achieved by the passage of a frontal system, which increases winds and instability in the regional air mass. We interpret PC4 as a rough measure of atmospheric mixing, as it is highly correlated with the formation and passage of low pressure systems. As high pressure systems build in the area, cold air drainage persists, limited land surface heating takes place, and thus limited atmospheric mixing occurs. During these high pressure systems, elevation and its quadratic have a complicated relationship with minimum temperature (Figure 10b), as the site is under inversion conditions. This phenomenon is well described by our model, and it is quantified by elevation, the quadratic of elevation, and their interaction with PC4. While the inclusion of these terms does not make for a perfect fitting model, it is a first step in attempting to incorporate better information about synoptic weather conditions and their relation to landscape scale temperature mapping.

2) Maximum temperature

As seen in Figure 4, regional air temperature is also highly correlated with T_{max} at the study site. Maximum temperatures tend to increase and decrease with the regional air mass. However, it is apparent that the range of maximum temperature values observed on a given day varies by season and synoptic weather conditions.

The lapse rate of maximum temperatures is much more consistent than that of minimum temperature (Figure 11 a), as cold air drainage is not a major component of the daytime climate at our study site. There is a strong effect of elevation and its quadratic interacting with the sin and cosine waves that were fit to the model, which indicates that the effects of elevation and its quadratic change with the seasons (table 4). This is easy to reconcile, as changes in the season also bring about changes in the sun angle. Much like in minimum temperature, high pressure coupled with low sun angles (hence low atmospheric mixing) during the winter months can lead to inversions in maximum daily temperature (Figure 11 b). The cosine curve better explains the seasonality of our study site. To further explain the seasonality of inversions, our maximum temperature model includes an interaction term of the cosine wave with the TCI at the study site. This helps to account for the fact that TCI is more predictive of T_{max} in our study site during the winter months, as this is when inversions are most likely to occur.

Aside from some extreme winter values (Figure 8, December 2013), the bias in the T_{max} model is relatively consistent. This is likely due to the stability and predictability of maximum temperatures throughout most of the year. Atmospheric lapse rates are reasonable averages of the distribution of maximum temperature throughout a landscape due to the stability of T_{max}. However, this overly simple approach still does not account for site specific differences in solar irradiance, canopy cover, and other important variables, thus the analyst must weight the importance of detailed landscape-scale temperature maps.

c. Effects of landscape features on near-surface temperature

1) Minimum temperature

Elevation is certainly one of the most important components of T_{min} distribution in the area, but the relationship is not a simple linear one. Our model accounts for numerous ways the effects of elevation on T_{min} vary throughout the landscape (Table 3), and we are likely still missing part of the picture. Allowing a quadratic term of elevation helps to account for the persistent cold air drainage encountered at our site, and will likely apply to other sites in the western United States or any arid, midlatitude site. While allowing for the quadratic term makes for a more complicated model interpretation, it helps to better model the actual system. Elevation and its quadratic also exhibit a strong interaction with canopy cover at the study site. While there is no direct evidence to support it, we speculate that this term helps to account for the varying structure of the canopy, as it changes dramatically at our study site with elevation.

Not surprisingly, there is a very weak effect of IRRAD on T_{min} at our study site. By the time daily minimum temperature occurs at our site, it is likely that most of the long-wave radiation has already escaped the ground surface. Canopy cover has a strong effect on minimum temperature at our study site, as thicker canopies tend to insulate the near-surface climate from extreme temperature swings. Our study confirms that this process is taking place at the Snake Range. One of the strongest landscape effects is the shape of the terrain and its effect on cold air drainage. Our model accounts for this effect by including TCI and terrain slope as model terms. These two variables have relatively strong effects. The effect of TCI is negative, as areas with high TCI values are typically concavities in the landscape. These concavities are areas that are likely to allow more dense cold air to accumulate, thus will generally display a colder climate than would areas with a more convex landscape all else held equal. Slope has a positive effect on T_{min}, as areas with higher slope values will ”clear” the more dense cold air rapidly as it cools, helping to keep these areas near the same temperature as the regional air mass.

2) Maximum temperature

Elevation has a strong effect on T_{max} in the Snake Range, with a relatively small effect displayed by the quadratic of elevation (e.g. Figure 11a). The strength of this relationship bodes well for applied scientists that have a need for general descriptions of maximum temperature in the region, as elevation data is readily available and highly predictive of temperature. However, this relationship is not stationary with time, as in the winter months, temperature inversions from the valley floor all the way to the mountain summit are not uncommon (e.g. Figure 11b). Thus, if the application requires detailed information about temperature or requires the ability to describe when and how deep inversions are in the study site, a method similar to what was employed in this study is suggested.

Incoming solar radiation has a very large effect on maximum temperature at the sites in the SRSN (Table 4). This is a very intuitive relationship, where sites and times with high solar radiation tend to show a higher maximum daily temperature and vice versa. Theoretical incoming solar radiation can be easily modeled within a GIS framework, making this important variable available to all applications. However, to better understand they dynamics of how inrradiance effects maximum temperature, it would be ideal to include information on cloud cover. On cloudy days or during the formation of summer thunder storms, the actual incoming solar radiation could greatly diverge from the theoretical value calculated with GIS.

As temperature inversions of T_{max} are not uncommon at our study site, particularly in the winter (not shown), we have included an interaction term of TCI, elevation, and the quadratic of elevation with the sine and cosine waves that describe seasonal variabion at our study site. Again, the cosine wave seems to better fit the timing of seasonality at our site. Allowing our landscape variables to interact with the day of year helps to account for the differing effect of these landscape variables through time. While TCI and ELEV^2 are both important variables to help describe inversion conditions, they do not contribute much information to the distribution of maximum temperature over the landscape during normal conditions. Ideally a better description of the seasonality at our site can be achieved, which will allow for better mapping of the timing and distribution of inversions in T_{max} in the Snake Range.

d. Refinements and future work

The availability and low cost of modern microsensors such as the LogTag Trix 16 units used in this study have led to a proliferation of landscape-scale temperature studies. These studies will benefit from some form of standardization, as it is currently quite difficult to compare results. Some researchers place their sensors in trees as we have, some place their sensors under the soil surface, some use PVC housings for radiation shields, and some make their own in house radiation shields. The amount of measurement error and bias that is contributed by these different methods needs to be taken into account when quantitatively comparing results, but the general drivers of near- surface air temperature in different geographic regions likely hold true.

It is important to note that while this model effectively describes near-surface temperature in the Snake Range throughout the period of record, researchers must be cautious if they are to extrapolate such models to larger landscapes or different time periods. While the use of the NCEP Reanalysis 1 data to describe synoptic conditions at our study site makes the model well suited for calculating temperature maps of past conditions, it is worth noting that the near-ground climate of the past may be very different than the near-ground climate of the present. This exercise would certainly hold some merit in a first glimpse of a detailed climate history for the area, but many of the assumptions made by this work will likely break in different points in space or time.

References

Adams, H. D., M. Guardiola-Claramonte, G. a. Barron-Gafford, J. C. Villegas, D. D. Breshears, C. B. Zou, P. a. Troch, and T. E. Huxman, 2009: Temperature sensitivity of drought-induced tree mortality portends increased regional die-off under global-change-type drought. *Proceedings of the National Academy of Sciences of the United States of America*, **106 (17)**, 7063–6, doi:10.1073/pnas.0901438106, URL http://www.pubmedcentral.nih.gov/articlerender.fcgi?artid=2678423\&tool=pmcentrez\&rendertype=abstract.

Ashcroft, M. B., and J. R. Gollan, 2011: Fine-resolution (25 m) topoclimatic grids of near-surface (5 cm) extreme temperatures and humidities across various habitats in a large (200 300 km) and diverse region. *International Journal of Climatology*, n/a–n/a, doi:10.1002/joc.2428, URL http://doi.wiley.com/10.1002/joc.2428.

Ashcroft, M. B., J. R. Gollan, D. I. Warton, and D. Ramp, 2012: A novel approach to quantify and locate potential microrefugia using topoclimate, climate stability, and isolation from the matrix. *Global Change Biology*, **18 (6)**, 1866–1879, doi:10.1111/j.1365-2486.2012.02661.x, URL http://doi.wiley.com/10.1111/j.1365-2486.2012.02661.x.

Barry, R. G., 2008: *Mountain Weather and Climate*. 3rd ed., Camabridge University Press, New York.

Bates, D and Maechler, M and Bolker, B and Walker, S, 2014: *lme4: Linear mixed-effects models using Eigen and S4*. URL http://CRAN.R-project.org/package=lme4.

Bivand, R. S., E. Pebesma, and V. Gomez-Rubio, 2013: *Applied Spatial Data Analysis with R*. 2nd ed., Springer, New York.

Blandford, T. R., K. S. Humes, B. J. Harshburger, B. C. Moore, V. P. Walden, and H. Ye, 2008: Seasonal and Synoptic Variations in Near-Surface Air Temperature Lapse Rates in a Mountainous Basin. *Journal of Applied Meteorology and Climatology*, **47 (1)**, 249–261, doi:10.1175/2007JAMC1565.1, URL http://journals.ametsoc.org/doi/abs/10.1175/2007JAMC1565.1.

Cabrera, H. M., F. Rada, and L. Cavieres, 1998: Effects of temperature on photosynthesis of two morphologically contrasting plant species along an altitudinal gradient in the tropical high Andes. *Oecologia*, **114 (2)**, 145–152, doi:10.1007/s004420050430, URL http://link.springer.com/10.1007/s004420050430.

Crimmins, S. M., S. Z. Dobrowski, J. a. Greenberg, J. T. Abatzoglou, and A. R. Mynsberge, 2011: Changes in climatic water balance drive downhill shifts in plant species' optimum elevations. *Science (New York, N.Y.)*, **331 (6015)**, 324–7, doi:10.1126/science.1199040, URL http://www.ncbi.nlm.nih.gov/pubmed/21252344.

Daly, C., M. Halbleib, and J. Smith, 2008: Physiographically sensitive mapping of climatological temperature and precipitation across the conterminous United States. *International Journal of Climatology of Climatology*, doi:10.1002/joc, URL http://onlinelibrary.wiley.com/doi/10.1002/joc.1688/full.

Diaz, H., M. Grosjean, and L. Graumlich, 2003: *Climate variability and change in high elevation regions: past, present and future*, Vol. 2001. 1–4 pp., URL http://link.springer.com/chapter/10.1007/978-94-015-1252-7_1.

Dobrowski, S. Z., J. T. Abatzoglou, J. a. Greenberg, and S. Schladow, 2009: How much influence does landscape-scale physiography have on air temperature in a mountain environment? *Agricultural and Forest Meteorology*, **149 (10)**, 1751–1758, doi:10.1016/j.agrformet.2009.06.006, URL http://linkinghub.elsevier.com/retrieve/pii/S0168192309001488.

ESRI, 2014: *ArcGIS 10.1*. URL http://resources.arcgis.com/en/help/main/10.1/index.html#//00nv0000000v000000.

Fridley, J. D., 2009: Downscaling climate over complex terrain: High finescale (<1000 m) spatial variation of near-ground temperatures in a montane forested landscape (Great Smoky Mountains). *Journal of Applied Meteorology and Climatology*, **48**, 1033–1049, doi:10.1175/2008JAMC2084.1.

Geiger, R., R. H. Aron, and P. Todhunter, 2009: *The Climate Near the Ground*. 7th ed., Rowman & Littlefield Publishers.

Hannachi, A., I. T. Jolliffe, and D. B. Stephenson, 2007: Empirical orthogonal functions and related techniques in atmospheric science: A review. *International Journal of* . . . , **27**, 1119–1152, doi:10.1002/joc, URL http://onlinelibrary.wiley.com/doi/10.1002/joc.1499/full.

Hijmans, R. J., 2014: *raster: raster: Geographic data analysis and modeling*. URL http://CRAN.R-project.org/package=raster, r package version 2.3-12.

Hijmans, R. J., S. E. Cameron, J. L. Parra, P. G. Jones, and A. Jarvis, 2005: Very high resolution interpolated climate surfaces for global land areas. *International Journal of Climatology*, **25 (15)**, 1965–1978, doi:10.1002/joc.1276, URL http://doi.wiley.com/10.1002/joc.1276.

Holden, Z. A., M. A. Crimmins, S. A. Cushman, and J. S. Littell, 2011: Empirical modeling of spatial and temporal variation in warm season nocturnal air temperatures in two North Idaho mountain ranges, USA. *Agricultural and Forest Meteorology*, **151 (3)**, 261–269, doi:10.1016/j.agrformet.2010.10.006, URL http://linkinghub.elsevier.com/retrieve/pii/S0168192310002819.

Holden, Z. A., A. E. Klene, R. F. Keefe, and G. G. Moisen, 2013: Design and evaluation of an inexpensive radiation shield for monitoring surface air temperatures. *Agricultural and Forest Meteorology*, **180**, 281–286, doi:10.1016/j.agrformet.2013.06.011, URL http://linkinghub.elsevier.com/retrieve/pii/S016819231300169X.

Horel, J. D., and X. Dong, 2010: An Evaluation of the Distribution of Remote Automated Weather Stations (RAWS). *Journal of Applied Meteorology and Climatology*, **49 (7)**, 1563–1578, doi:10.1175/2010JAMC2397.1, URL http://journals.ametsoc.org/doi/abs/10.1175/2010JAMC2397.1.

Kalnay, E., and Coauthors, 1996: The NCEP/NCAR 40-Year Reanalysis Project. *Bulletin of the American Meteorological Society*, **77 (3)**, 437–471.

Lookingbill, T., and D. Urban, 2003: Spatial estimation of air temperature differences for landscape-scale studies in montane environments. *Agricultural and Forest Meteorology*, **114**, 141–151, URL http://www.sciencedirect.com/science/article/pii/S016819230200196X.

Lundquist, J. D., and D. R. Cayan, 2007: Surface temperature patterns in complex terrain: Daily variations and long-term change in the central Sierra Nevada, California. *Journal of Geophys-

ical Research, **112 (D11)**, 1–15, doi:10.1029/2006JD007561, URL http://www.agu.org/pubs/crossref/2007/2006JD007561.shtml.

Lundquist, J. D., N. Pepin, and C. Rochford, 2008: Automated algorithm for mapping regions of cold-air pooling in complex terrain. *Journal of Geophysical Research*, **113 (D22)**, D22 107, doi:10.1029/2008JD009879, URL http://doi.wiley.com/10.1029/2008JD009879.

Martinec, J., and a. Rango, 1986: Parameter values for snowmelt runoff modelling. *Journal of Hydrology*, **84 (3-4)**, 197–219, doi:10.1016/0022-1694(86)90123-X, URL http://linkinghub.elsevier.com/retrieve/pii/002216948690123X.

McCune, B., and D. Keon, 2002: Equations for potential annual direct incident radiation and heat load. *Journal of vegetation science*, **(1966)**, 603–606, URL http://onlinelibrary.wiley.com/doi/10.1111/j.1654-1103.2002.tb02087.x/abstract.

Mensing, S., and Coauthors, 2013: A Network for Observing Great Basin Climate Change. *Eos, Transactions American Geophysical Union*, **94 (11)**, 105–106, doi:10.1002/2013EO110001, URL http://doi.wiley.com/10.1002/2013EO110001.

Millar, C. I., N. L. Stephenson, and S. L. Stephens, 2007: Climate change and forests of the future: Managing in the face of uncertainty. **17 (8)**, 2145–2151.

Myrick, D. T., and J. D. Horel, 2008: Sensitivity of Surface Analyses over the Western United States to RAWS Observations. *Weather and Forecasting*, **23 (1)**, 145–158, doi:10.1175/2007WAF2006074.1, URL http://journals.ametsoc.org/doi/abs/10.1175/2007WAF2006074.1.

Pebesma, E., 2012: spacetime: Spatio-Temporal Data in R. *Journal of Statistical Software*, **51 (7)**, 1–30, URL http://www.jstatsoft.org/v51/i07/.

Pepin, N., D. Benham, and K. Taylor, 1999: of Northern in the Maritime Rates Uplands Modeling Lapse England : for Climate Change Implications. *Arctic, Antarctic, and Alpine Research*, **31 (2)**, 151–164.

Pepin, N. C., C. Daly, and J. Lundquist, 2011: The influence of surface versus free-air decoupling on temperature trend patterns in the western United States. *Journal of Geophysical Research*, **116 (D10)**, D10 109, doi:10.1029/2010JD014769, URL http://doi.wiley.com/10.1029/2010JD014769.

Pinheiro, J., D. Bates, S. DebRoy, D. Sarkar, and R Core Team, 2014: *nlme: Linear and Nonlinear Mixed Effects Models*. URL http://CRAN.R-project.org/package=nlme, r package version 3.1-118.

R Core Team, 2014: *R: A Language and Environment for Statistical Computing*. Vienna, Austria, R Foundation for Statistical Computing, URL http://www.R-project.org/.

Rolland, C., 2003: Spatial and seasonal variations of air temperature lapse rates in Alpine regions. *Journal of Climate*, **16**, 1032–1046, URL http://journals.ametsoc.org/doi/abs/10.1175/1520-0442(2003)016⟨1032:SASVOA⟩2.0.CO;2.

Steinhauser, F. W., 1967: Methods of Evaluation and Drawing of Climate Maps in Mountainous Countries. *Archiv fur Meteorologie, Geophysik und Bioklimatologie*, **15 (4)**, 329–358.

Thornton, P. E., S. W. Running, and M. a. White, 1997: Generating surfaces of daily meteorological variables over large regions of complex terrain. *Journal of Hydrology*, **190 (3-4)**, 214–251, doi:10.1016/S0022-1694(96)03128-9, URL http://linkinghub.elsevier.com/retrieve/pii/S0022169496031289.

LIST OF TABLES

TABLE 1. Summary statistics for the EOF analysis conducted on SLP anomolies for the years 1958-2014. Only the first 4 of 544 EOFs are shown.

	EOF1	EOF2	EOF3	EOF4
Standard Deviation	120.14	92.90	63.92	54.60
Proportion of Variance	0.36	0.22	0.10	0.08
Cumulative Proportion of Variance	0.36	0.58	0.68	0.76

TABLE 2. Table of the predictor variables used in models of maximum and minimum near-surface air temperature.

Variable	Description	Units	Range in Snake Range	Source of Derivation
Tair	Daily mean temperature at 700 hPa level	$^{\circ}$C		NCEP Reanalysis 1
PC4	Daily fluctuations in SLP			EOF analysis of daily SLP
ELEV	Elevation (AMSL)	m	1560-3850	30-m digital elevation model
TCI	Terrain Convergence Index	Unitless	2.1-17-1	GIS based on elevation (r.terraflow in GRASS)
IRRAD	Daily shortwave radiation	MWm^2	0.378-9.81	GIS based on terrain, location, season (r.sun in GRASS)
CC	Canopy cover	%	0-72	USGS NLCD product
SLOPE	Terrain slope	$^{\circ}$	0-73.3	Based on elevation model
JDAY	Day of year (1-365)			

TABLE 3. Fixed effect coefficients of minimum daily temperature model for the SRSN.

Coefficient	Estimate	Standard Error	t value
(Intercept)	-36.07	10.27	-3.51
IRRAD	0.002	0.02	0.10
ELEV	32.60	8.46	3.85
$ELEV^2$	-6.87	1.61	-4.25
PC4	0.13	0.02	5.96
T_{air}	0.88	0.02	55.23
TCI	-0.16	0.07	-2.36
CC	1.05	0.245	4.22
SLOPE	0.04	0.02	2.57
$\cos(2\pi/365 * \mathrm{JDAY})$	-1.78	0.18	-9.69
$\sin(2\pi/365 * \mathrm{JDAY})$	-0.17	0.12	-1.41
ELEV:PC4	-0.09	0.02	-5.24
$ELEV^2$:PC4	0.01	0.002	4.42
ELEV:CC	-0.80	0.20	-3.96
$ELEV^2$:CC	0.14	0.04	3.68

TABLE 4. Fixed effect coefficients of maximum daily temperature model for the SRSN.

	Estimate	Std. Error	t value
(Intercept)	31.98	6.66	4.80
T_{air}	0.87	0.02	35.68
IRRAD	0.58	0.03	21.96
PC4	-0.01	0.00	-5.62
ELEV	-10.91	5.49	-1.99
ELEV^2	0.37	1.03	0.36
TCI	-0.07	0.07	-1.00
cos(2π/365 * JDAY)	-0.70	0.96	-0.73
sin(2π/365 * JDAY)	-0.43	0.96	-0.45
SLOPE	0.03	0.02	1.95
CC	0.01	0.01	1.13
TCI:cos(2π/365 * JDAY)	0.02	0.01	3.34
TCI:sin(2π/365 * JDAY)	0.00	0.01	0.21
ELEV:cos(2π/365 * JDAY)	-3.61	0.71	-5.06
ELEV^2:cos(2π/365 * JDAY)	1.08	0.14	7.75
ELEV:sin(2π/365 * JDAY)	1.13	0.72	1.57
ELEV^2 :sin(2π/365 * JDAY)	-0.32	0.14	-2.26

TABLE 5. Model bias for daily maximum and daily minimum temperature models described in text. Bias is calculated as predicted temperature minus observed temperature. Average bias per month at each NevCAN station (Figure 1) are displayed here as well as overall average bias for the entirety of the time series.

Month	Jun	Jul	Aug	Sep	Oct	Nov	Dec	Jan	Feb	Mar	Apr	May	Overall
							Minimum Temperature Bias						
Sage	1.80	0.27	0.47	-2.24	1.24	1.33	5.56	2.47	-0.81	0.09	-0.98	0.77	0.85
PJ	2.88	1.69	1.98	-0.82	2.76	3.57	7.69	4.05	0.72	1.63	0.51	2.29	2.43
Montane	-0.54	0.07	-0.74	-0.54	-0.16	0.05	1.21	-0.33	-0.32	0.51	0.13	0.12	-0.05
Subalpine	-0.61	-0.06	-0.10	-1.14	-0.84	-0.30	-0.41	-1.70	-0.97	0.55	0.30	0.36	-0.40
Overall	0.53	0.49	0.40	-1.19	0.75	1.16	3.51	1.12	-0.34	0.70	-0.01	0.88	0.69
							Maximum Temperature Bias						
Sage	-0.89	0.25	-0.35	-0.11	-1.73	0.51	3.92	-0.01	-0.73	-1.04	-0.17	0.71	0.05
PJ	-4.27	-3.14	-3.78	-3.58	-5.16	-2.82	0.64	-3.34	-4.17	-4.57	-3.67	-2.72	-3.36
Montane	-4.75	-3.10	-3.86	-2.40	-3.37	-2.33	-3.61	-3.71	-3.40	-3.00	-2.96	-2.31	-3.22
Subalpine	-3.55	-1.55	-2.36	-0.32	-1.62	-0.05	-1.83	-1.63	0.34	-0.16	-0.22	-0.22	-1.12
Overall	-3.20	-1.88	-2.59	-1.60	-2.97	-1.17	-0.22	-2.17	-1.99	-2.19	-1.75	-1.13	-1.92

TABLE 6. Model MAE

Site	Jun	Jul	Aug	Sep	Oct	Nov	Dec	Jan	Feb	Mar	Apr	May	Overall
Minimum Temperature MAE													
Sage	2.98	1.78	2.32	2.50	3.98	2.73	6.15	4.82	2.77	2.70	2.56	2.49	3.16
PJ	1.58	1.65	1.87	1.64	1.85	1.76	1.85	2.00	2.55	1.88	2.11	1.43	1.84
Montane	1.08	1.14	1.28	1.14	1.47	0.83	1.61	1.25	1.43	1.46	1.31	1.30	1.27
Subalpine	1.02	0.82	0.80	1.44	1.67	1.55	1.88	2.14	1.70	1.57	1.54	1.17	1.43
Overall	1.56	1.35	1.57	1.68	2.24	1.72	2.87	2.55	2.11	1.90	1.88	1.60	1.92
Maximum Temperature MAE													
Sage	1.90	1.35	1.33	2.23	2.53	3.14	4.68	1.95	2.48	1.86	2.03	1.75	2.27
PJ	2.86	2.14	2.47	2.84	3.19	3.04	1.81	2.32	2.47	2.54	2.96	2.40	2.59
Montane	4.64	3.47	4.04	3.45	3.73	2.94	3.70	3.71	3.69	3.50	3.80	3.38	3.69
Subalpine	3.60	2.07	2.79	2.34	2.93	2.63	2.84	2.68	2.35	2.21	2.00	2.03	2.56
Overall	3.36	2.26	2.65	2.72	3.10	2.94	3.26	2.67	2.75	2.53	2.70	2.39	2.78

TABLE 7. RMSE Table

Site	Jun	Jul	Aug	Sep	Oct	Nov	Dec	Jan	Feb	Mar	Apr	May	Overall
							Minimum Temperature RMSE						
Sage	3.72	2.23	2.89	3.06	4.56	3.35	8.00	5.76	3.56	3.22	3.13	3.05	4.18
PJ	2.04	1.90	2.33	1.99	2.28	2.01	2.25	2.60	2.96	2.41	2.54	1.93	2.28
Montane	1.40	1.49	1.51	1.41	1.86	1.11	2.21	1.63	2.00	2.29	2.09	1.65	1.75
Subalpine	1.34	1.13	1.02	1.73	1.97	1.99	2.35	2.54	2.16	2.36	2.26	1.45	1.91
Overall	2.19	1.74	2.07	2.14	2.89	2.26	4.46	3.50	2.74	2.60	2.54	2.11	2.70
							Maximum Temperature RMSE						
Sage	2.55	1.76	1.79	2.81	2.90	4.11	5.64	2.52	2.95	2.20	2.55	2.52	3.04
PJ	3.35	2.54	2.74	3.41	3.54	3.66	2.16	2.76	3.24	2.93	3.32	2.81	3.07
Montane	5.06	3.94	4.35	3.82	4.05	3.34	4.03	4.05	4.32	4.05	4.22	3.86	4.13
Subalpine	3.96	2.46	3.06	2.81	3.28	3.37	3.53	3.26	2.76	2.49	2.40	2.44	3.04
Overall	3.92	2.79	3.12	3.24	3.47	3.63	4.04	3.20	3.37	3.00	3.21	2.96	3.35

LIST OF FIGURES

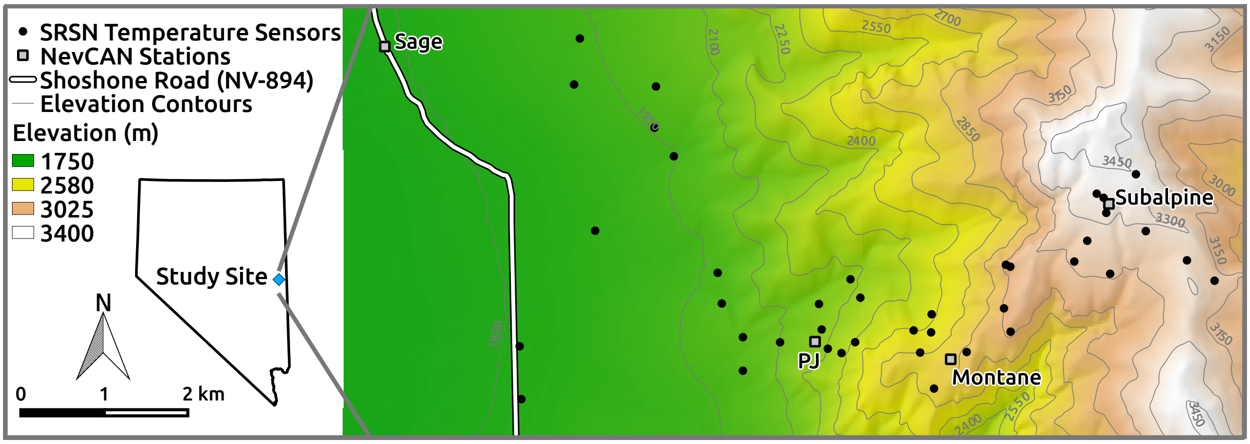

FIG. 1. A map of the study site in the Snake Range, Nevada, USA. The blue diamond indicates the location of this study within the state of Nevada. The Snake Range Sensor Network (SRSN) locations are shown as black points on the map and the NevCAN weather stations are indicated by the gray squares and labeled by name. Colored shading indicates elevation, the gray lines are elevation contours spaced at 150 m, and the white line represents Shoshone Road (NV-894).

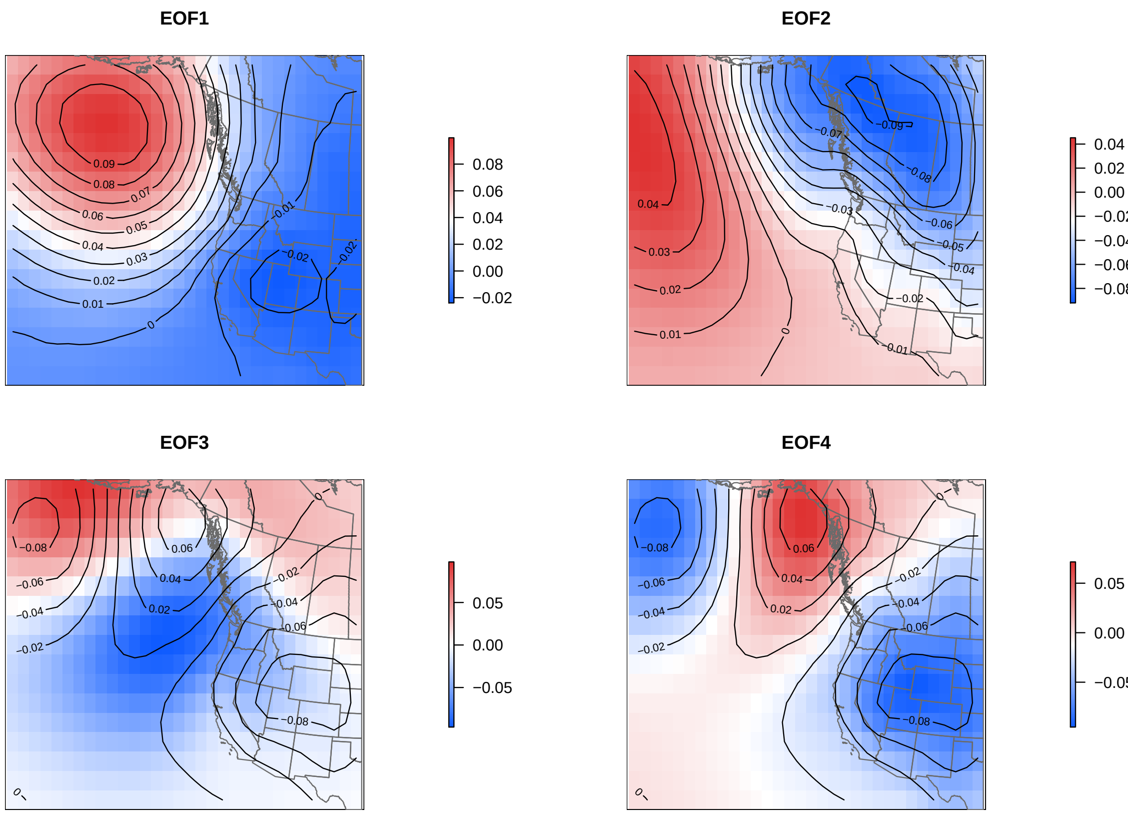

FIG. 2. The first 4 of 544 empirical orthogonal functions (EOFs) identified by an empirical orthogonal function analysis of daily mean sea level pressure (SLP) anomalies. Physical interpretation of these EOFs can be found in text. The variation of these spatial patterns through time as Principle Components (PCs) can be observed in Figure 3, where the numeric label of each PC corresponds to the numeric label of these EOFs.

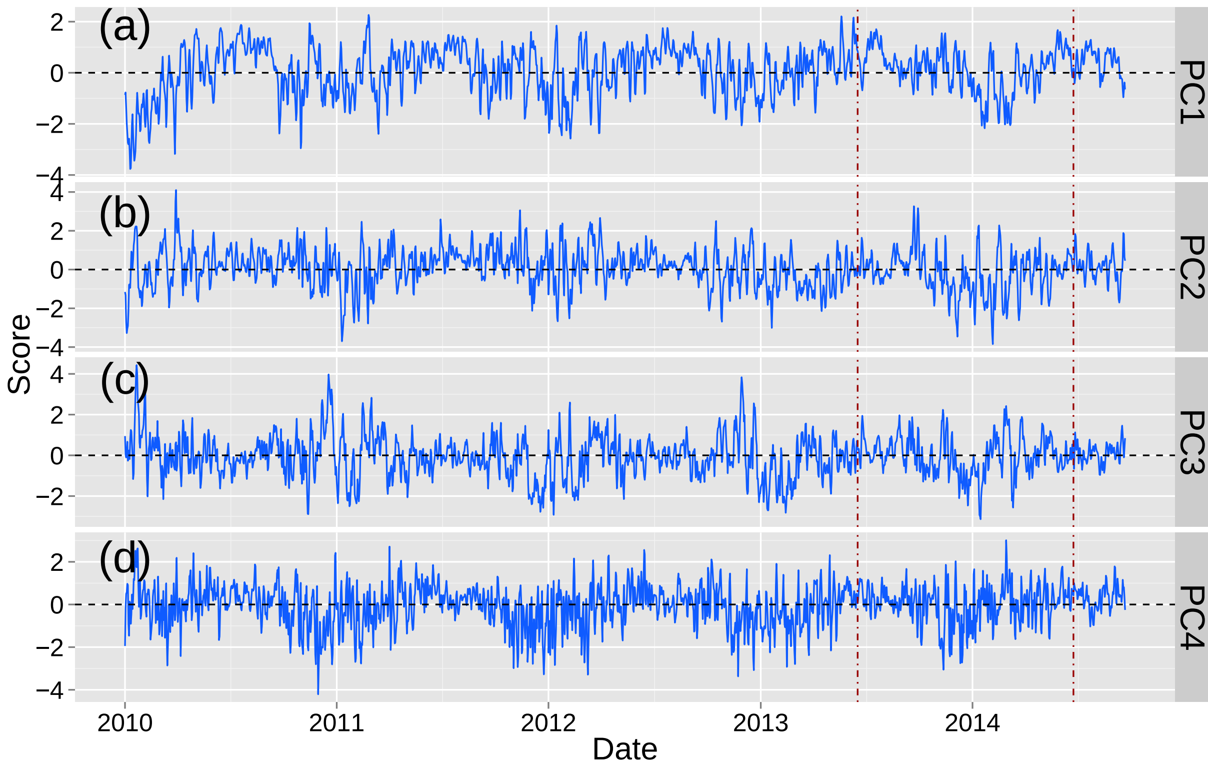

831 FIG. 3. The first 4 of 544 principle components (PCs) identified and described in text. A temporal subset
832 spanning 1 January 2009 to the final day of the analysis period, 24 September 2014, is displayed for clarity.
833 Also note the differing y-axes, as the PC scores are relative. The vertical red lines indicate the portion of the
834 time series that coincides with the Snake Range Sensor Network analysis period.

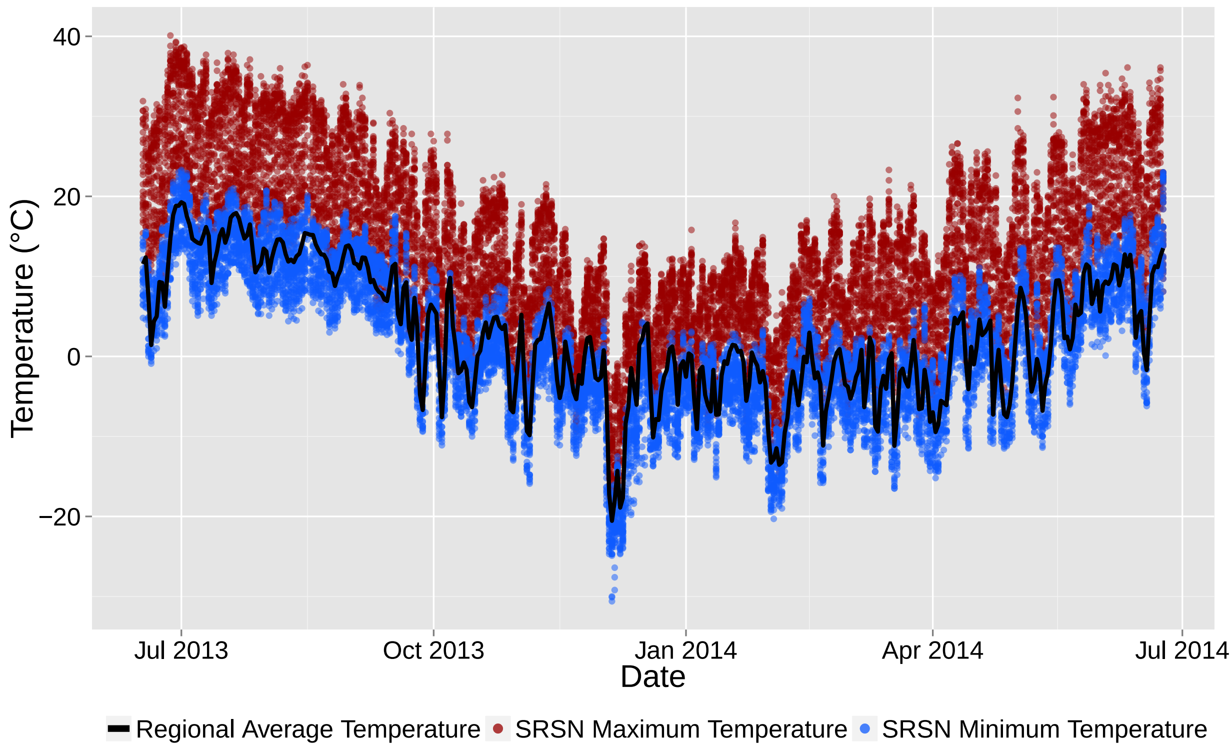

835 FIG. 4. A time series showing all SRSN maximum and minimum daily temperature data collected during the
836 study period (17 June 2013 to 24 June 2014) as red and blue symbols, respectively, and the NCEP Reanalysis 1
837 daily average air temperature at the 700 hPa level drawn as a black line. All of the SRSN T_{max} and T_{min} data are
838 plotted for each day, thus up to 80 dots are present on each day. We intentionally chose color the data by sites
839 for simplicity of viewing.

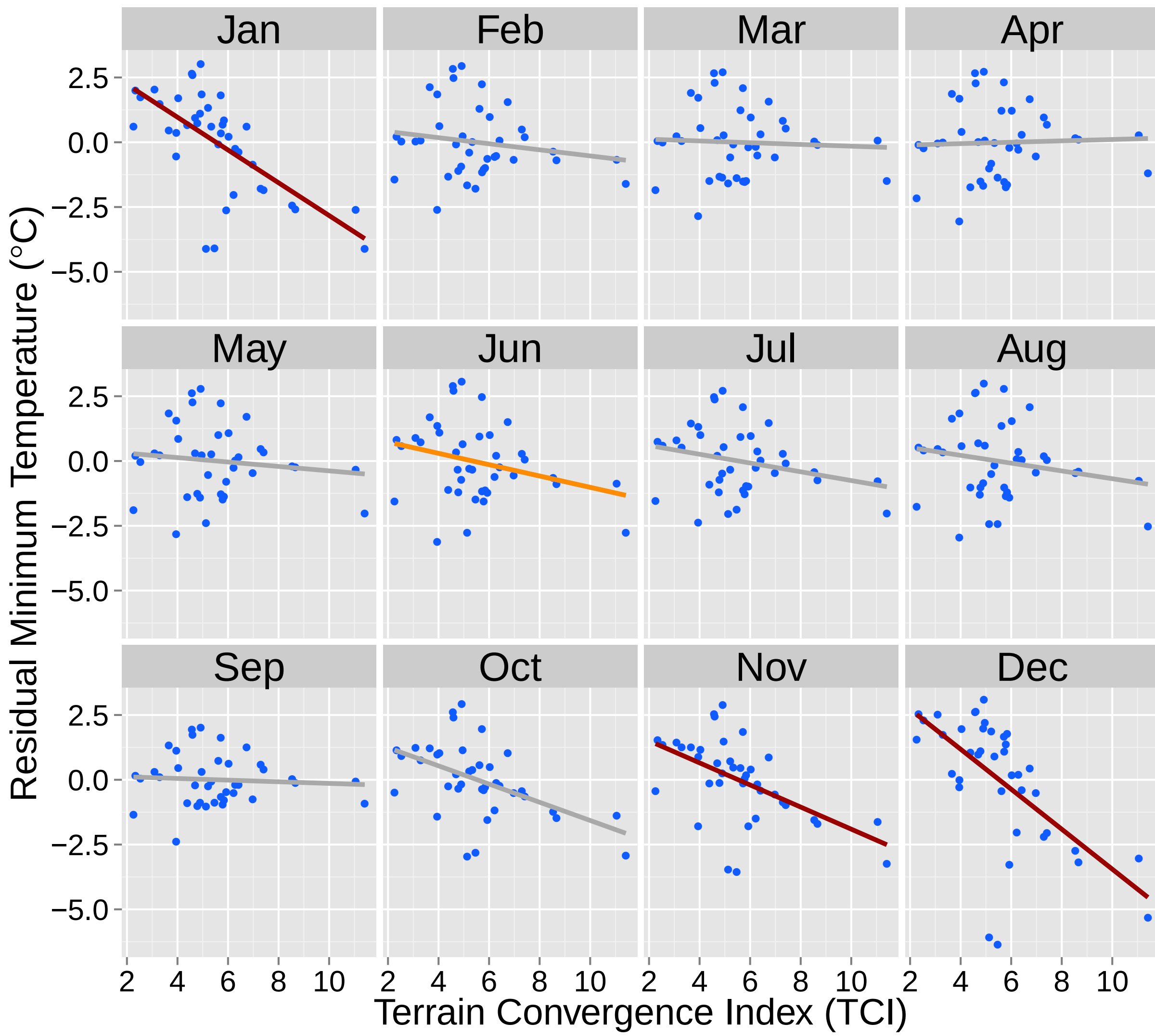

FIG. 5. Modeling of minimum daily temperature averaged over the course of a month between 17 June 2013 and 24 June 2014 expressed as a function of terrain convergence index (TCI). Temperature is expressed as the residual of a mixed-effect model fit to the entirety of the SRSN data predicted solely by elevation with random intercepts by month. Residuals were then averaged for each site per month, and plotted against the TCI value at each sensor. The lines are fit by least squares regression. Lines are colored by the p-value associated with these least square regressions, where red indicates significance at the 0.05 level ($p < 0.05$), orange indicates significance at the 0.10 level ($p < 0.10$), and gray indicates no significance at the 0.10 level ($p > 0.10$).

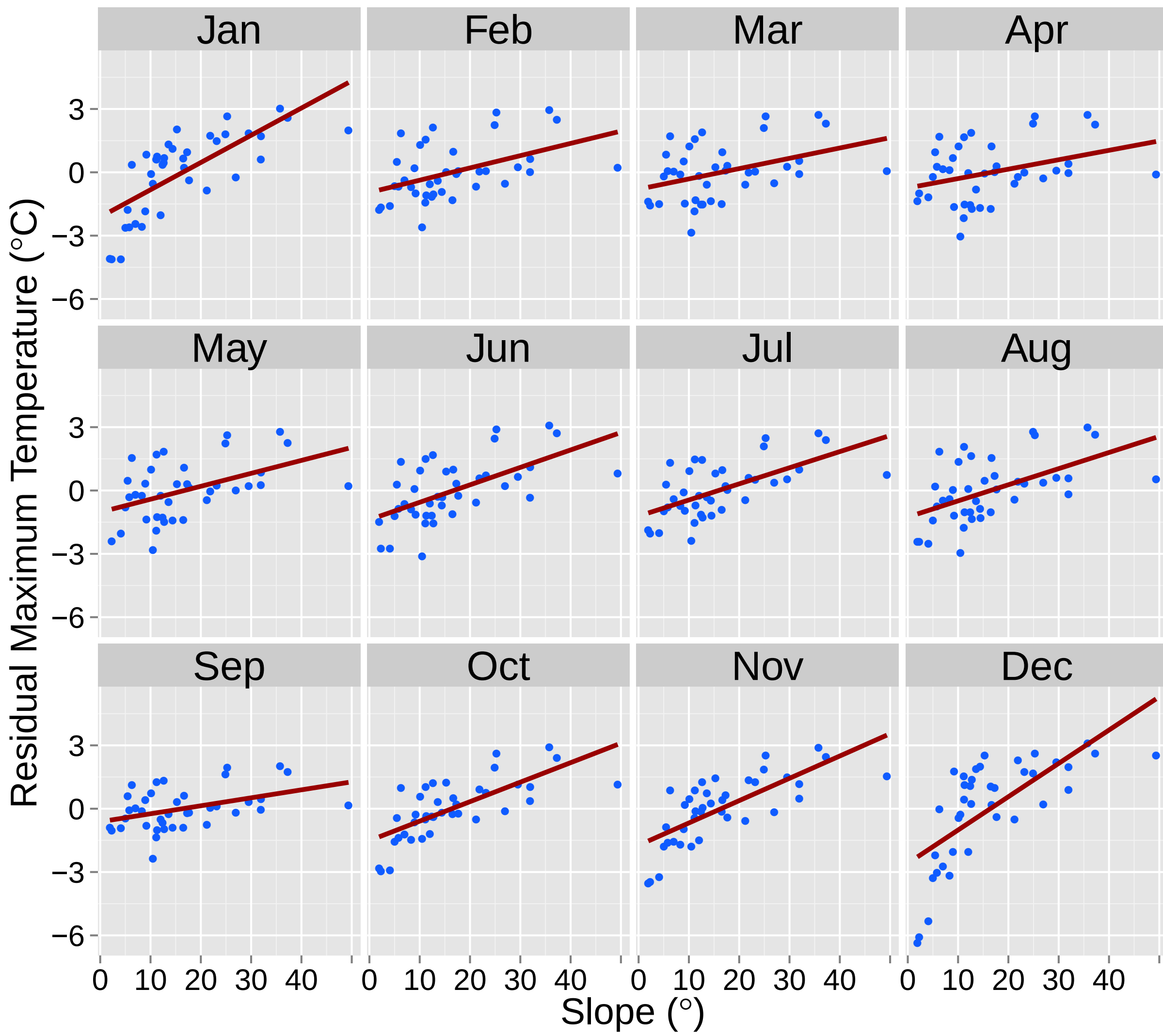

847 FIG. 6. Modeling of maximum daily temperature averaged over the course of a month between 17 June 2013
848 and 24 June 2014 expressed as a function of terrain slope (°). Temperature is expressed as the residual of a
849 mixed-effect model fit to the entirety of the SRSN data predicted by elevation with random intercepts by month.
850 Residuals were then averaged for each site per month and plotted against the terrain slope at each sensor. The
851 lines are fit by least squares regression. All months were statistically significant at the 0.05 level (p ¡ 0.05).

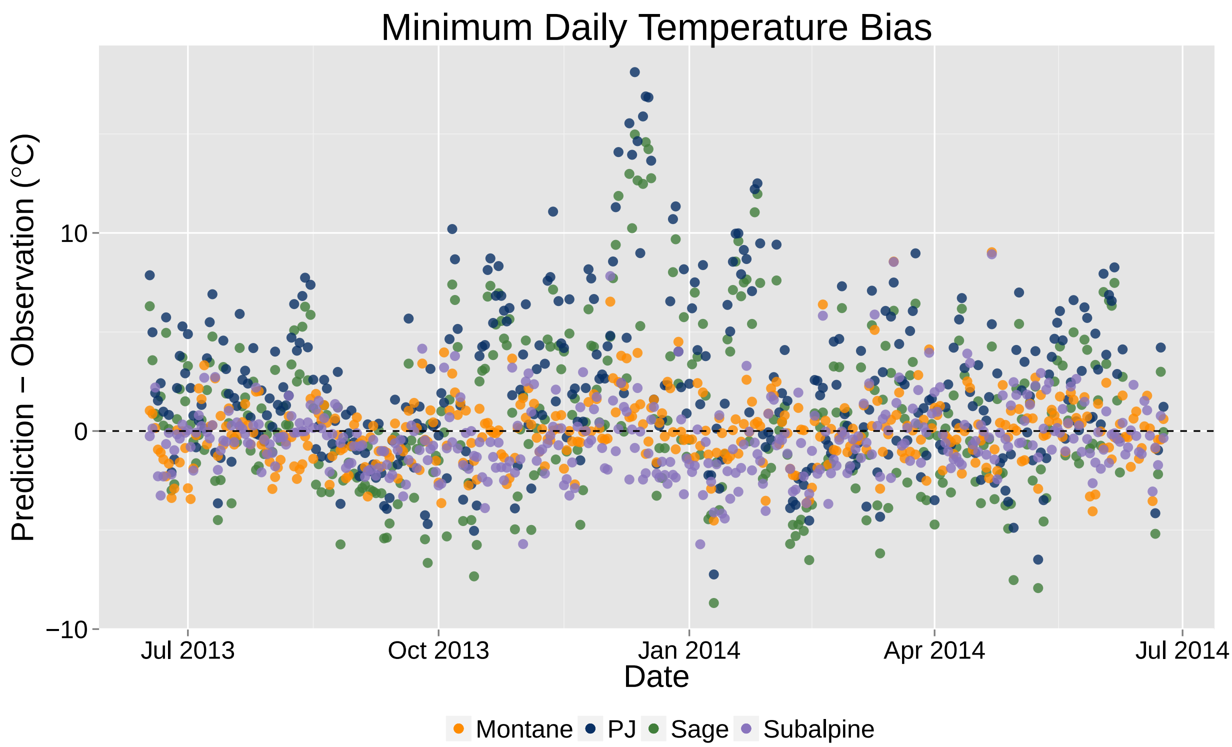

852 FIG. 7. Difference between daily minimum temperature (°C) as predicted by the hierarchical mixed-effects model described in text and observed daily minimum temperature at 4 NevCAN stations over time. The Montane site is visualized as orange dots, the Pinyon-Juniper site (PJ) is dark blue, the Sagebrush (Sage) site is dark green, and the Subalpine site is purple. The black horizontal line represents a perfect prediction.

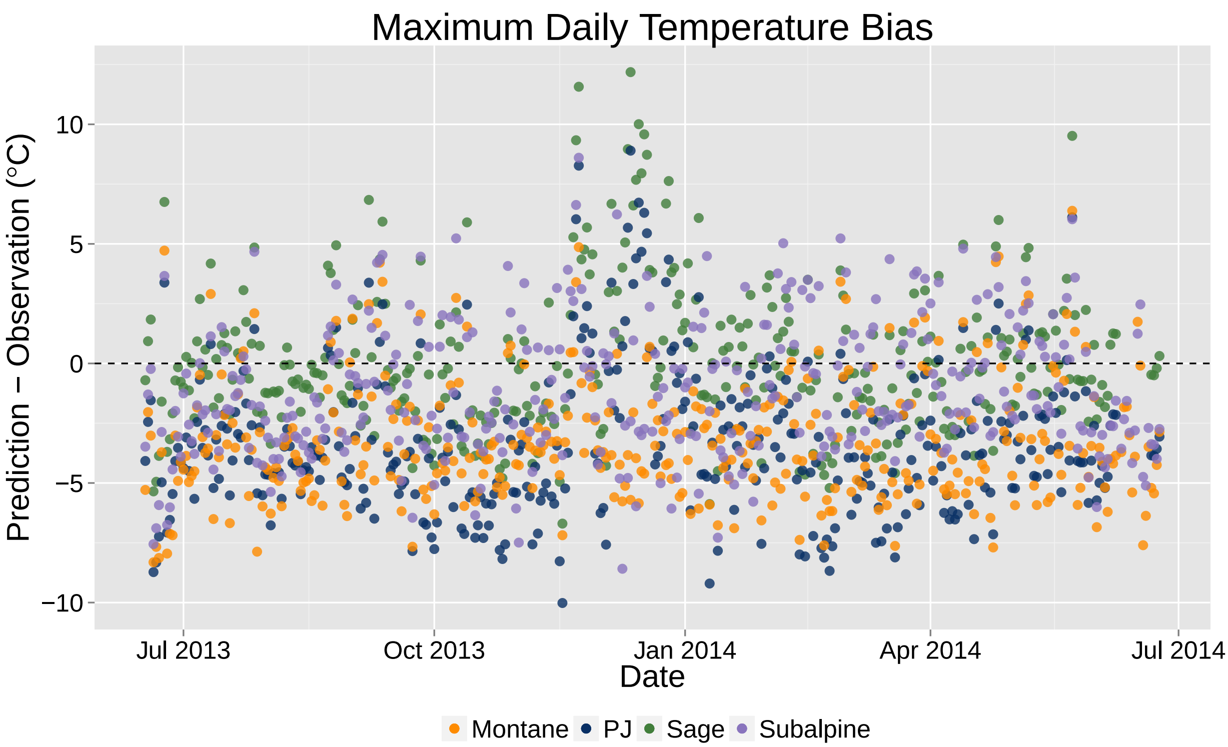

856 FIG. 8. Difference between daily maximum temperature (°C) as predicted by the hierarchical mixed-effects
857 model described in text and observed daily maximum temperature at 4 NevCAN stations over time. The Montane
858 site is visualized as orange dots, the Pinyon-Juniper site (PJ) is dark blue, the Sagebrush (Sage) site is dark green,
859 and the Subalpine site is purple. The black horizontal line represents a perfect prediction.

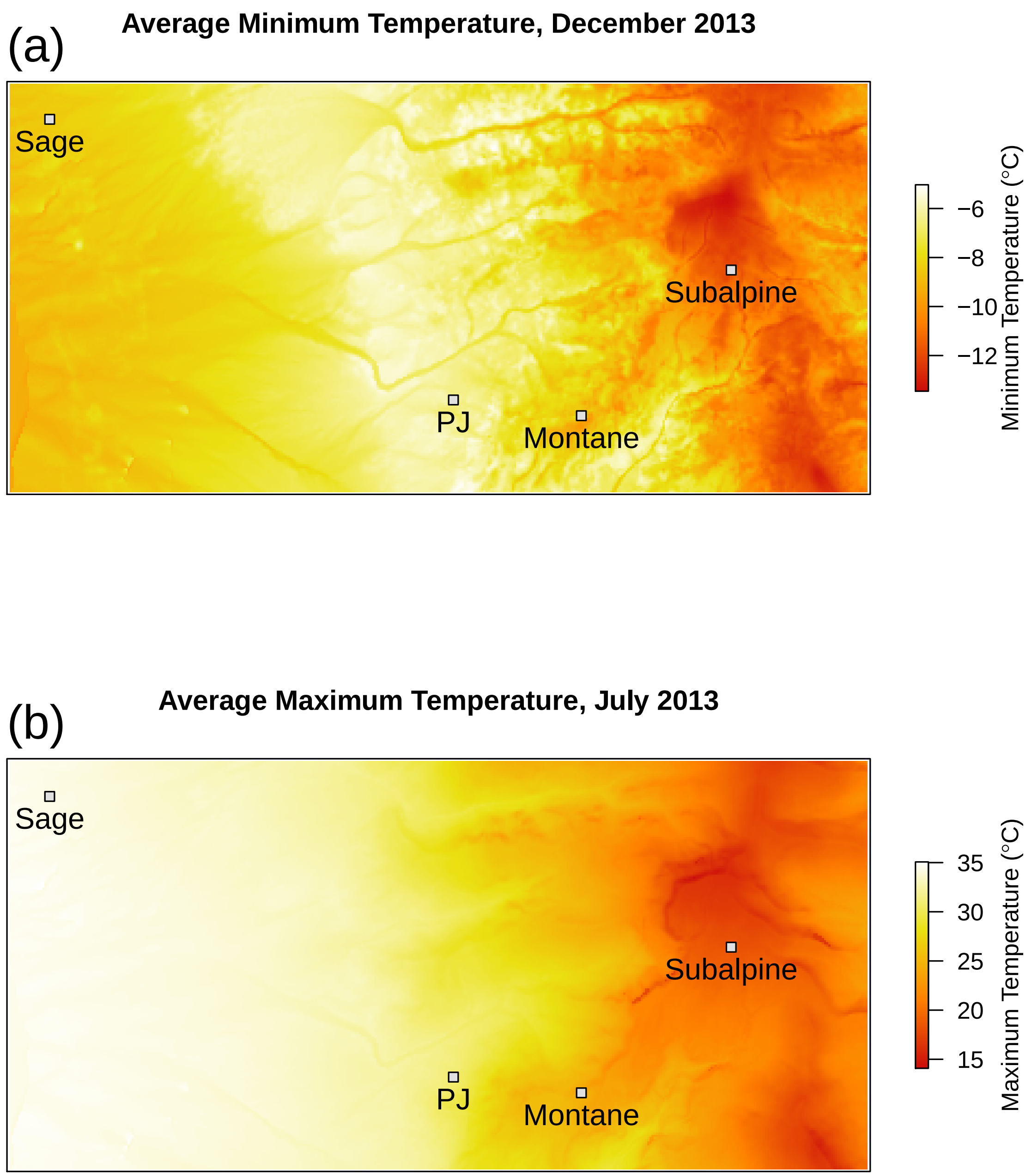

FIG. 9. Two maps of temperature as predicted by the models described in text. Gray squares indicate NevCAN stations, which were used as validation sites in this work. Scale and orientation are the same as Figure 1. Note that (a) and (b) have different legends and are for different time periods. (a) A map of average minimum temperature throughout the study site, calculated by taking the mean of daily minimum temperature for the month of December 2013. (b) A map of average maximum temperature, calculated by taking the mean of daily maximum temperature predictions for the month of July 2013.

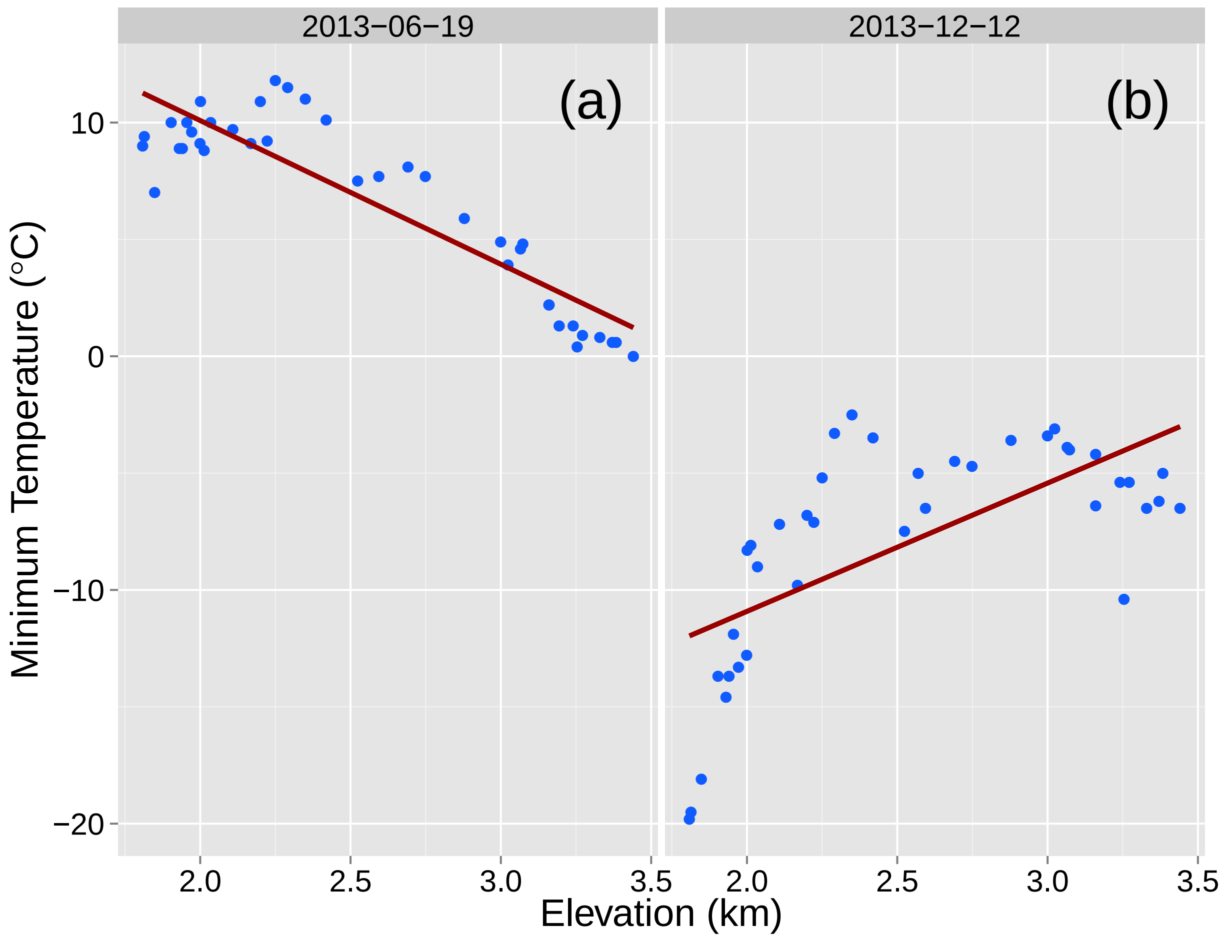

FIG. 10. Minimum temperature across the 40 sites of the SRSN on two separate days plotted against site elevation. The panel on the left is from 2013 June 19, and it displays the more typical pattern of T_{min} for the area. Minimum temperature at the lower elevation sites is relatively constant, as cold air drainage occurs on a nearly nightly basis at the site. The right pane shows minimum temperature recorded by the SRSN plotted against elevation. This particular day shows a deep inversion present at the study site, where temperature increases with elevation rather than decreases. The red lines represent a least squares linear regression model that has been fit to the data, which is often thought of as the lapse rate.

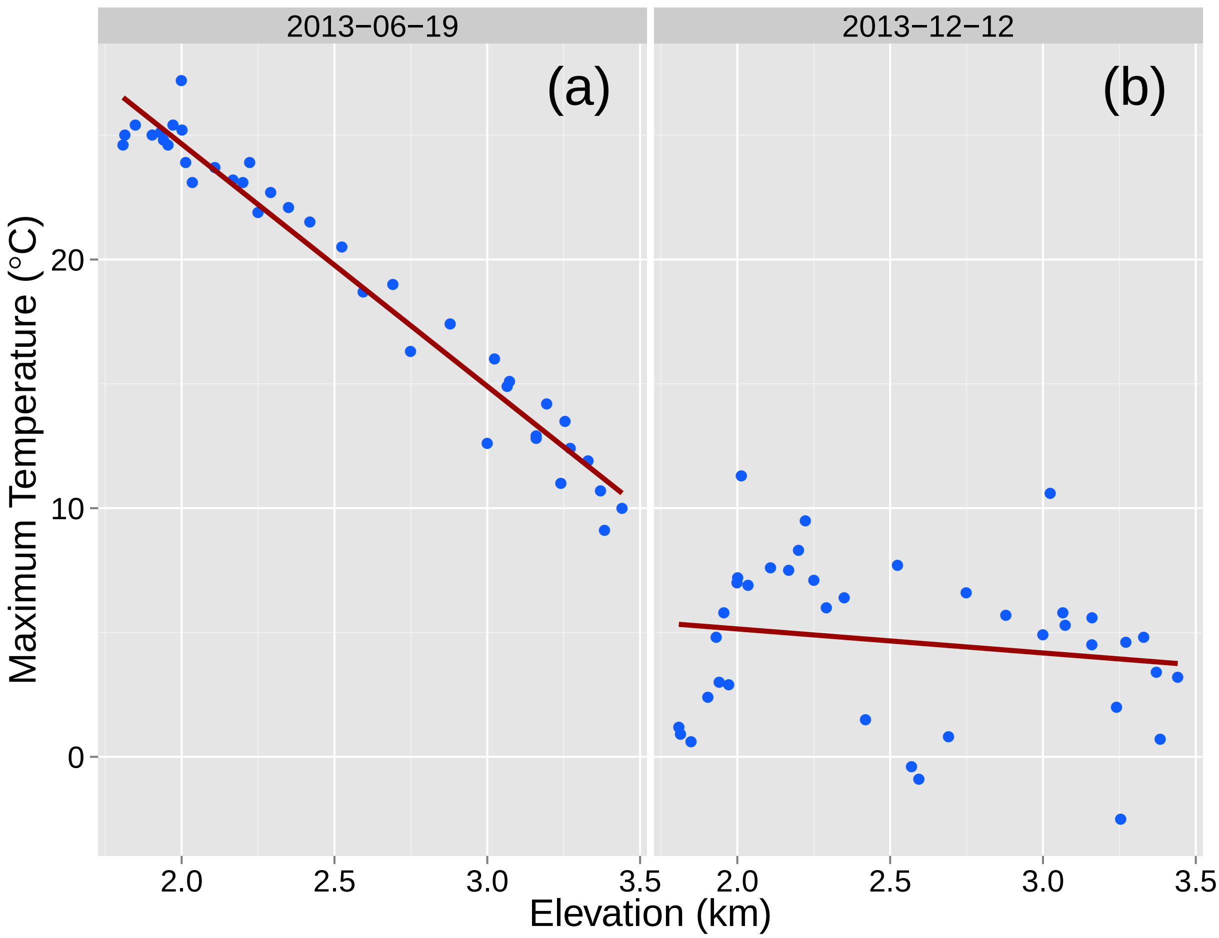

FIG. 11. Maximum temperature across the 40 sites of the SRSN on two separate days plotted against the elevation of each site, where red lines represent a least squares linear regression line fitted to the data, which is often thought of as the atmospheric lapse rate. (a) Maximum daily temperature from 2013 June 19. this displays a typical maximum temperature observation at the site, where maximum temperature decreases linearly with decreasing elevation. (b) Maximum daily temperature from 2013 December 12, which shows a persistent inversion occurring at the site. As you increase elevation, there is a very slight decrease in maximum temperature for that day.